Hindawi
Advances in Civil Engineering
Volume 2022, Article ID 7408393, 16 pages
https://doi.org/10.1155/2022/7408393

Research Article

Integrity Testing of a Platform-Pile System Using a Sensor Array and Wavenumber Domain Analysis

Minghui Fu [1] **and Meihong Lin** [1,2]

[1]*Department of Applied Mechanics and Engineering, Sun Yat-Sen University, Guangzhou, 510275, China*
[2]*CCCC Fourth Harbor Engineering Institute Co., Ltd., Guangzhou 510000, China*

Correspondence should be addressed to Minghui Fu; stsfmh@mail.sysu.edu.cn

Received 13 March 2022; Revised 11 June 2022; Accepted 13 June 2022; Published 7 July 2022

Academic Editor: Liborio Cavaleri

Appropriate impact and sensor locations must be chosen in pile integrity tests to prevent three-dimensional effects caused by the torsional and flexural modes. The three-dimensional characteristics cause high-frequency interference, especially in bridge and wharf piles. A method is required to minimize the high-frequency interference without reducing the accuracy of the pile integrity test. A multivelocity integrity test method is proposed based on a sensor array and frequency-wavenumber (FK) domain analysis to eliminate high-frequency interference and reduce the errors in the output of integrity tests of platform-pile systems. FK filtering is performed to eliminate the spatial alias frequency and separate the upward and downward wavefield and the vibration modes in an integrity test of a platform-pile system. The optimum sensor location to minimize the influence of interference signals is at the bending plane relative to the impact location. Using a sensor array reduces the influence of the sensor location on the test results and minimizes the requirements for determining the location of the excitation point and sensors in the traditional low-strain integrity testing (LST) method, thereby improving the applicability of this method.

1. Introduction

Assessing elastic wave propagation in structures is a highly promising technique for structural health monitoring (SHM) in civil engineering. The integrity assessments of pile foundations of bridges and wharves remain a significant challenge in superstructures with a lack of construction information [1, 2]. Pile integrity assessments are crucial for reinforcement and reconstruction [3]. The oxidation of steel rebars, chloride-induced steel corrosion, and the resulting degradation of concrete threaten the integrity of pile systems in marine environments [4, 5]. The coupled effects of current scour and wave load can cause deformation of the pile-soil system, causing damage to the structural components (such as piles and beams) and ultimately leading to structural instability of wharves, and the changes in environmental conditions (such as geological parameters) caused by wave and current scour make pile inspections vital [6, 7]. Due to the large number of overlapping reflected waves generated by complex structures, SHM with guided waves is complicated. A sparse array of transducers has been used for performance evaluations of structures in the presence of large noise [8, 9], but few studies focused on using sparse arrays for SHM of platform piles in soil.

Low-strain integrity testing (LST) has been utilized to assess the structural health of piles in soil for decades. The piles are subjected to an impact force at the pile head in an impulse response test, and the reflected wave signals are analyzed to evaluate the damage [10, 11]. In the traditional LST method, the optimal distance between the striking point and the receiver is 0.5R-0.7 R when the impact location is on the top surface of the pile [12–14]. However, wave interference occurs in superstructures, making it difficult to distinguish the damage from the pile toe signals in the reflected wave [15]. Three-dimensional (3D) wave effects caused by superstructures result in significant interference with the pile-soil vertical responses [16, 17]. When there is no impact location at the pile head, the results of a lateral

impact are influenced by the reflected signals generated by the superstructure, complicating the use of LST for pile inspection.

Parallel seismic (PS) tests have provided excellent results [2, 18, 19] because the pile bottom can be identified by an inflection point in the stacked trace plots. A correction equation based on the wave velocity and pile-borehole distance has been proposed to improve the estimation accuracy [20]. An equation was also proposed to compensate for the borehole inclination [21]. A mathematical algorithm that considers the soil layers and borehole inclination was put forward [22], and the ray-tracing method was used to identify defects in a pile using the PS method [23]. Compared with the widely used LST method, the PS method has the advantage of being applicable to the integrity testing of superstructure piles. The sensors are placed by drilling a hole in the soil, but the complexity of layered soil may complicate the detection. Using a lateral horizontal impact has been suggested as a more feasible approach for assessing pile foundations of superstructures [24, 25]. Although PS tests have been used to determine the length and integrity of piles using the first arrival time and waveforms [19, 26], this method is limited by complex soil parameters, and a borehole must be drilled to place the sensors.

The frequency-wavenumber (FK) method has been used for wavefield transformations of vertical seismic profiles [27] and damage imaging [28–30]. Structural features and defects can be accurately imaged using frequency band-pass and wavenumber band-pass filters [31]. The traditional LST method typically uses only one or two sensors for the integrity testing of piles. Since the FK method requires large amounts of sensor data, few studies used this method for the LST of piles.

The finite element method has been used to analyze PS test data, and a length correction method has been proposed [20]. The elastodynamic finite integration technique (EFIT) is a more accurate and stable time-domain method for wave propagation analysis in elastic media [32–35] than the boundary element method (BEM) method [36, 37] and finite element method [38]. The 3D characteristics of superstructures can be computed and analyzed using the boundary conditions of the piles in the soil. Therefore, the EFIT method is well suited for analyzing composite computational problems of platform piles in soil.

The objectives of this study were to develop a strategy to reduce the errors in the output of integrity tests of platform-pile systems using sensors, determine the effect of high-frequency modes, and improve the applicability of the traditional LST method for platform-pile systems. We propose an analysis method for platform-pile systems using a sensor array and wavenumber domain analysis for assessing the pile integrity. A filtering window function and FK analysis are used for wavefield separation after conducting integrity testing of piles in soil. The performance and reliability of the method are evaluated using experiments and numerical analysis. The results of the integrity analysis of different impaction locations and sensor locations indicate that the method can deal with the high-frequency modes caused by the pile cap. The proposed method minimizes the requirements for determining the location of the impact and sensors in traditional LST methods, improving their applicability.

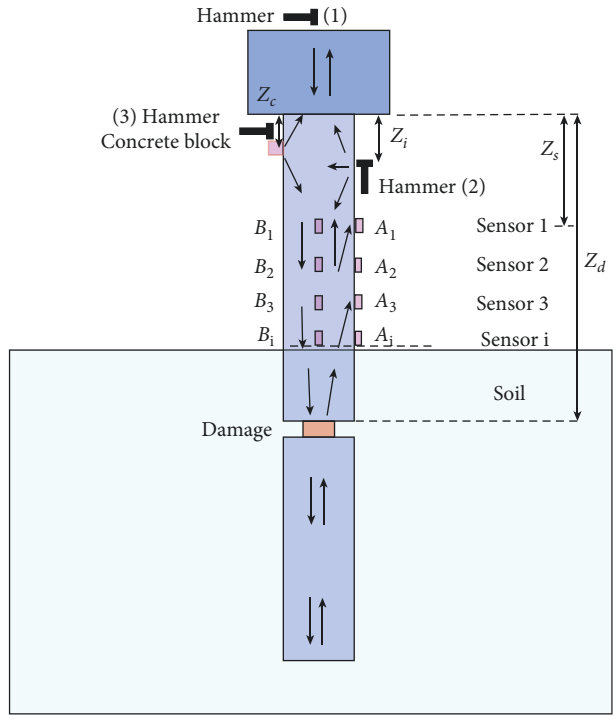

Figure 1: Sensor configuration during pile integrity testing.

2. Methodology

2.1. Sensor Array Configuration in Pile Integrity Testing. Few studies analyzed the use of LST of piles using a sensor array. However, it is necessary to understand the 3D effects caused by the torsional and flexural modes on stress wave propagation and develop a methodology to minimize the high-frequency interference without reducing the detection accuracy of pile integrity testing. The traditional LST method is not well suited for platform-pile systems due to the interference of the reflected wave of the upper structure with that of the lower structure. When the impact location is at the pile top of a superstructure, two wavefields propagate in different directions, i.e., the upward wavefield and the downward wavefield. The proposed method uses the FK filtering wavefield algorithm to separate the upward wavefield from the downward wavefield.

The sensors were placed on the lateral surface of the pile in the length direction, as shown in Figure 1. There were two groups of sensors, A_i and B_i, and three impact locations: (1) top impact, (2) lateral impact, and (3) impact on the concrete block. The concrete impact block can be quickly prefabricated and installed using epoxy resin and has strong applicability for on-site inspections.

The foundation pile with a cap was connected to the superstructure and underground rock mass, forming a vibration system. Structural cross-sectional differences and wave impedance changes occur at the connections, causing

vibration reflection. The internal defects of the pile also change the wave impedance and cause wave scattering. The change in the wave impedance at the interface between a defect and the pile has the following characteristics: the greater the change in the section, the more significant the defect is, the stronger the scattered energy is, and the lower the frequency of the scattered wave is. The travel time of the scattered wave is related to the defect location. The farther the distance, the longer the travel time is. A multichannel receiving system was used to track the downward wavefield of the superstructure and the upward wavefield of the lower defects to determine their respective locations and filter out the downward wavefield. The damage locations can be determined according to the energy and travel time of the reflected wave signal.

2.2. FK Wavefield Algorithm. The signals of a sensor array can be expressed as a binary function of the distance z and time t.

$$v = v(z,t). \tag{1}$$

A Fourier transform is applied to equation (1) to obtain the two-dimensional spectrum $V(k,\omega)$ [27], which is expressed as follows:

$$V(k,\omega) = \iint e^{i(\omega t - kz)} v(z,t)\mathrm{d}z\mathrm{d}t, \tag{2}$$

$$v(z,t) = \iint e^{-i(\omega t - kz)} V(k,\omega)\mathrm{d}k\mathrm{d}\omega, \tag{3}$$

where $v(z,t)$ is the time-domain velocity data measured at A_i or B_i. The two-dimensional spectrum $V(k,\omega)$ of $v(z,t)$ can be obtained by a Fourier transform. When a sensor array is used, Eqs. (2) and (3) are discretized and expressed as follows:

$$V(k,f) = \frac{1}{MN}\sum_{p=0}^{M-1}\sum_{q=0}^{N-1} v(p,q)e^{i2\pi(k(p/M)+f(q/N))}, \tag{4}$$

$$v(p,q) = \sum_{k=-A}^{k=A}\sum_{f=-B}^{f=B} V(k,f)e^{-i2\pi(k(p/M)+f(q/N))}, \tag{5}$$

where k is the wavenumber relative to z and f is the frequency relative to time t. M is the number of sensors, and N is the size of time-domain velocity data; p is the index of the sensors, and q is the index of the time-domain velocity data. $[-A, A]$ is the frequency range of k, and $[-B, B]$ is the range of f.

2.3. FK Filtering with a Window Function. Low and high wavenumber passband cutoffs were used as a filter for wavefield separation to remove all other wavenumbers within the frequency bandwidth of the excitation signal [28, 39]. However, due to the reflection of the pile cap, reflected waves with different wave velocities are generated, and the interference wave signals cannot be separated effectively by this method. Thus, it is necessary to use a window function for wave velocity filtering to separate the wave signals with different wave velocities. The following filter function is applied to equation (4) to remove all other data outside the bandwidth of the signal:

$$\widetilde{V}(k,f) = W_k(k,f)V(k,f). \tag{6}$$

The window function is expressed as follows:

$$W_k(k,f) = f\left(\frac{(k-f)}{C_0}\right), \tag{7}$$

where f is the window function, such as a rectangular window and Hann window; C_0 is the slope of the band signal relative to the wave velocity. For example, the Hann window is defined as follows:

$$f\left(\frac{(k-f)}{C_0}\right) = f(x) = \begin{cases} 0.5\left[1-\cos\left(\pi\dfrac{|x|}{D_r}\right)\right], & |x| \le D_r, \\ 0, & \text{otherwise.} \end{cases} \tag{8}$$

2.4. Spatial Alias Frequency Elimination. During the FK domain calculation, a spatial alias frequency is generated due to the irregular sampling locations of the sensor array and sparse spatial sampling. The spurious frequency leads to frequency dispersion; thus, the upward wavefield cannot be obtained, and the damage cannot be identified. Several processing techniques have been used to eliminate spatial alias frequency and prevent irregular sampling, such as channel interpolation. Processing the wave velocity data with a spatial alias frequency filter ensures that the damage can be detected in the wavefield data. De-aliasing and normalization of the sensor array data are a challenging problem in damage identification. Curvelet transform has been used as a rapid calculation method to improve efficiency [40]. In addition, the curved wave transformation algorithm has been developed [41]. The Hilbert–Huang transform (HHT) algorithm has been used for signal filtering [42]. Due to the characteristics of the sensor array data, we use a modified algorithm based on the HHT to filter out the spatial alias frequency signal.

The process of removing the spatial alias frequency is as follows:

(1) The local maximum and minimum points are detected in the input noise signal.

(2) The maximum and minimum points are removed in the wavelength bandwidth.

(3) The average and standard deviation of the amplitude and period of the spatial alias frequency signal are calculated. If the standard deviation is less than the set value, the maximum value and minimum value in the bandwidth are interpolated according to the adjacent feature points; otherwise, no interpolation is performed.

(4) The curve $c_i(k)$ is drawn using a cubic spline interpolation function.

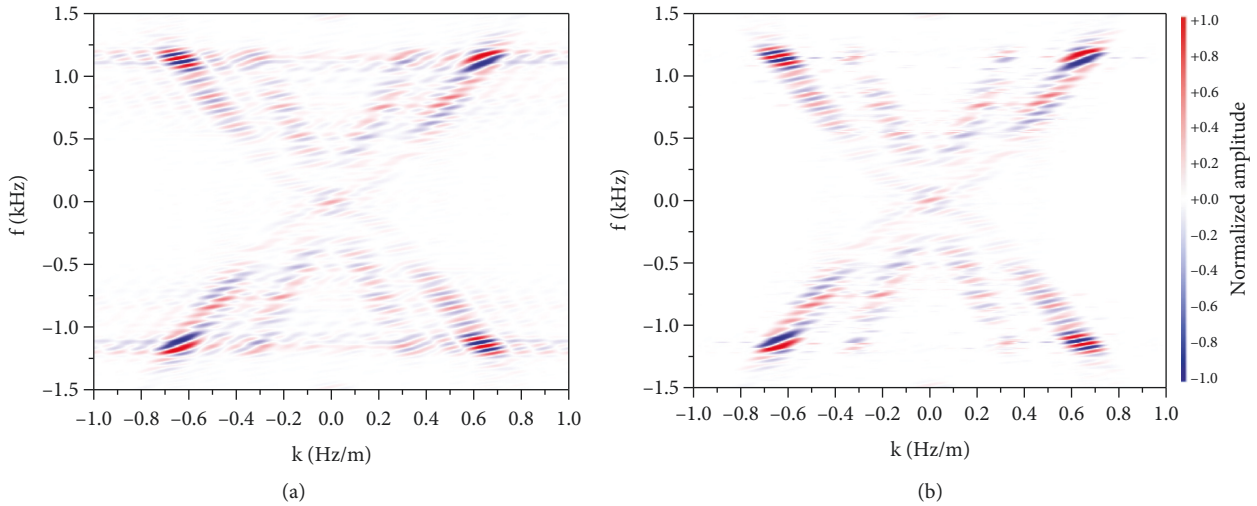

Figure 2: Raw data in the f-k domain before (a) and after (b) eliminating the spatial alias frequency signal. (a) Raw data in the f-k domain. (b) Data in the f-k domain after elimination.

(5) $c_i(k)$ is subtracted from the original data clock; the remaining signal $r_i(k)$ is obtained.

(6) Steps (1)-(5) are repeated until the root-mean-square (RMS) values of $c_i(k)$ and $r_i(k)$ are less than the preset value.

$$V\left(k, f_j\right) = \sum_{i=1}^{N} c_i(k) + r_N(k),\ j = [-B, B], \tag{9}$$

$$\begin{aligned} \mathrm{RMS}_{c_i(k)} &= \left[\int c_i(k)^2 \mathrm{d}k\right]^{(1/2)}, \\ \mathrm{RMS}_{r_i(k)} &= \left\{\int \left[r_i(k) - r_{i-1}(k)\right]^2 \mathrm{d}k\right\}^{1/2}. \end{aligned} \tag{10}$$

We remove the spatial alias frequency signal $\sum_{i=1}^{N} c_i(k)$, and then,

$$V\left(k, f_j\right) = r_N(k). \tag{11}$$

An example of the raw data in the f-k domain before and after eliminating the spatial alias frequency signal example is shown in Figure 2.

2.5. Frequency-Wavenumber Analysis. The propagation direction of the upward wavefield is opposite to that of the downward wavefield; thus, this feature can be used for wavefield separation. Fourier transformation is used to transform the $v(p, q)$ function of the distance z and time t into the $V(k, f)$ function of the wavenumber k and frequency f. In the plane of the $V(k, f)$ function, the slope represents the wave velocity. The velocity of the upward wavefield is positive (or negative), and the velocity of the downward wavefield is negative (or positive). If filtering is performed separately in the FK domain, wavefield separation can be performed by extracting positive or negative

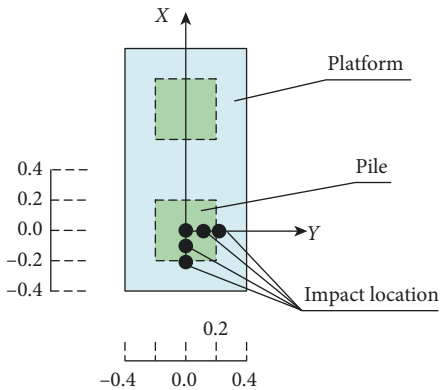

Figure 3: Impact locations of the two-pile model.

wavefield data and performing a two-dimensional inverse Fourier transform to obtain the upward wavefield $v(z, t)$.

$$V(k, f) = V^+(k, f) + V^-(k, f), \tag{12}$$

where $V^+(k, f)$ and $V^-(k, f)$ are the FK spectra of the upward and downward wavefields. Then,

$$\begin{aligned} v^+(z, t) &= \iint e^{-i\left(\omega t - k_z z\right)} V^+(k, \omega) \mathrm{d}k_z \mathrm{d}\omega, \\ v^-(z, t) &= \iint e^{-i\left(\omega t - k_z z\right)} V^-(k, \omega) \mathrm{d}k_z \mathrm{d}\omega, \end{aligned} \tag{13}$$

where $v^+(z, t)$ and $v^-(z, t)$ are the time-domain data of the upward and downward wavefields.

3. Wavefield Simulation with EFIT

3.1. Elastic Wave Equation. 3D ultrasonic EFIT simulations aid in understanding unexpected features to provide insight into mode conversion as Lamb waves interact with damaged areas [43]. Many authors have used EFIT for ultrasonic damage detection [34, 44]. According to Hooke's law and

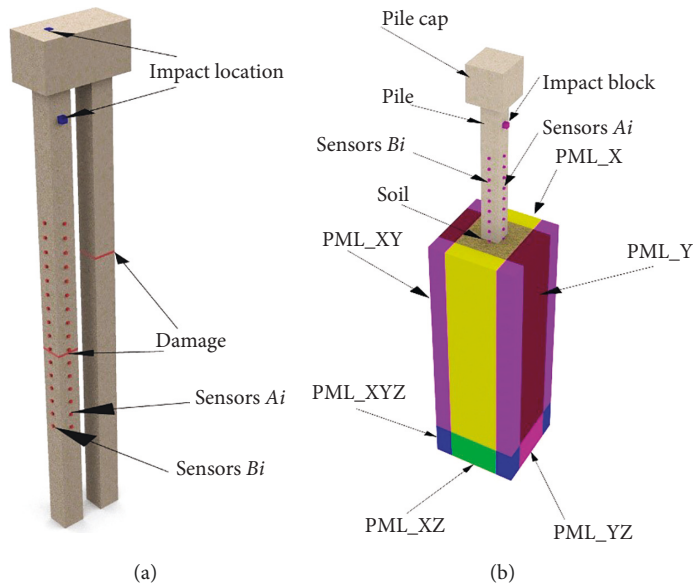

Figure 4: Computational domains. (a) The two-pile model. (b) The pile-soil model.

Cauchy's equation of motion, the 3D elastic wave equations can be written as follows using the summation convention for repeated subscripts:

$$\rho \dot{u}_i = \tau_{ij,j} + f_i,$$
$$\dot{\sigma}_{ij} = \lambda \dot{\epsilon}_{kk} \delta_{ij} + 2\mu \dot{\epsilon}_{ij}, k = x, y, z, \tag{14}$$

where $\tau_{ij,j} = (\partial \tau_{ij}/\partial x_j), \dot{\epsilon}_{xx} = (\partial u/\partial x), \dot{\epsilon}_{yy} = (\partial v/\partial y), and\ \dot{\epsilon}_{zz} = (\partial w/\partial z)$.

It is assumed in the computational model that the pile-soil system consists of linear elastic materials during LST. We use the (2M)th-order finite-difference scheme to calculate the temporal derivatives of the velocity and stress components and calculate the spatial derivatives with fourth-order staggered finite-difference (SFD) schemes to improve the accuracy [45, 46]. The heterogeneous finite-difference scheme is implemented following Moczo et al. (2002) [47].

3.2. Initial Conditions. An impact force $p(t)$ is applied to the impact surface as follows:

$$p(t) = \begin{cases} \dfrac{I}{t_0}\left(1 - \cos\dfrac{2\pi}{t_0}t\right), & (t \le t_0), \\ 0, & (t > t_0), \end{cases} \tag{15}$$

where I is the unit impulse of the force and t_0 is the contact time. The stress (τ_{zz} or τ_{yy}) values in the impact area are determined by the pressure $P = p(t)/(\pi r^2)$, and r is the radius of the impact surface.

3.3. Free-Surface Boundary Condition. Zero stress must be satisfied on the free-surface boundaries. The stress imaging technique is used for the free-surface treatments [46, 48].

Table 1: Parameters of the two-pile model.

Name	Value
Size of the pile section	400 × 400 mm
Pile length	8.0 m
Size of the pile cap	1.6 × 0.8 × 0.8 m
Damage location	z = 5.3–5.34 m
The side length of the concrete impact block	0.12 m
Location of concrete impact block	Z_c = 0.5 m

Table 2: Parameters of the two-pile model.

Material	E (GPa)	Poisson's ratio	ρ (kg/m^3)
Concrete	35	0.24	2400
Damaged wood	8	0.30	850

Note. The wood is shown in Figure 5, and the size of the middle hole is 13 × 13 cm.

Table 3: Parameters of the pile-soil model.

Name	Value
Size of the pile section	400 × 400 mm
Pile length	8.0 m
Size of the pile cap	0.8 × 0.8 × 0.8 m
Damage location	z = 5.0–5.2 m

Table 4: Parameters of the pile-soil model.

Material	E (GPa)	Poisson's ratio	ρ (kg/m^3)
Pile and cap	35	0.24	2400
Damage	10	0.30	2000

$$\sigma_{xx} = \tau_{xy} = \tau_{xz} = 0,$$
$$\sigma_{yy} = \tau_{xy} = \tau_{yz} = 0, \tag{16}$$
$$\text{or } \sigma_{zz} = \tau_{xz} = \tau_{yz} = 0.$$

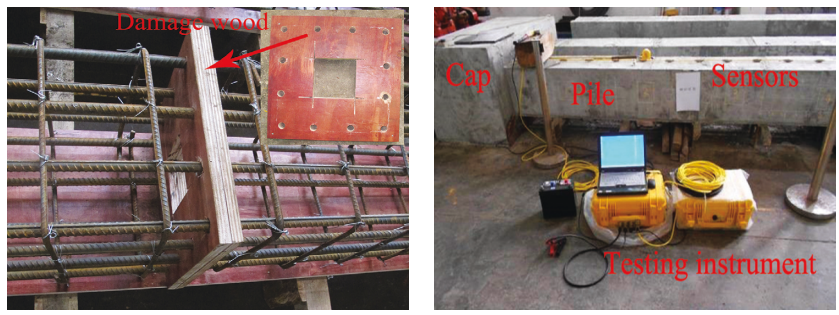

(a) (b)

Figure 5: Experimental test setup. (a) The damage of the two-pile model. (b) Testing instrument.

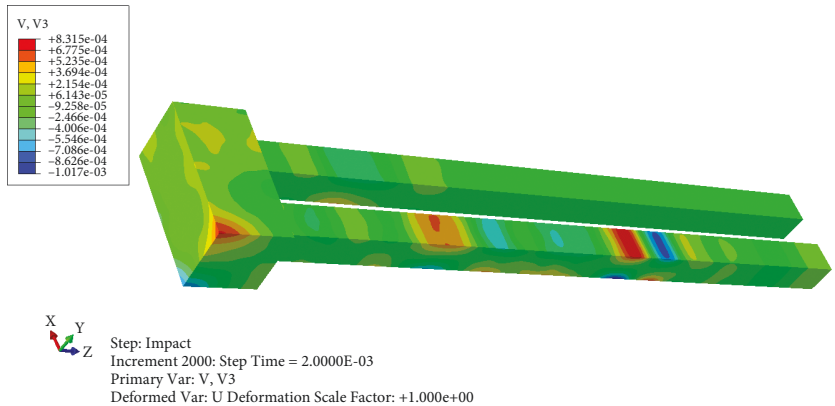

Figure 6: Abaqus model (time $t = 2$ ms).

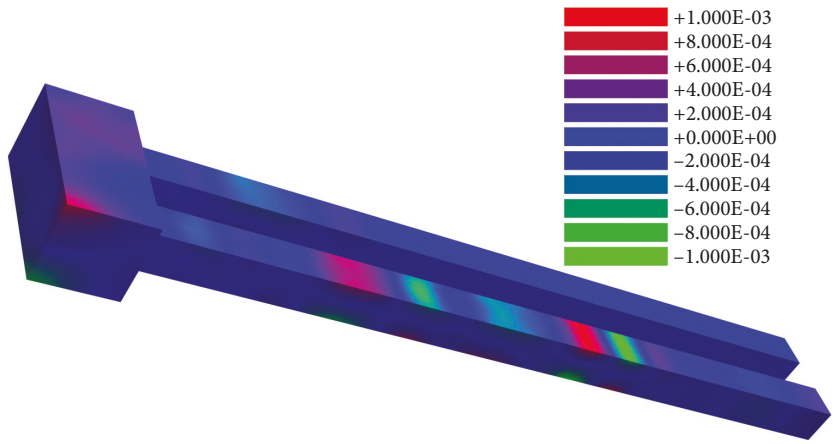

Figure 7: EFIT model (time $t = 2$ ms).

3.4. Perfectly Matched Layer Technique. The velocity stress of a perfectly matched layer (PML) is used to eliminate the reflection of the waves at the boundaries [49], and the maximum damping value d_0 is calculated as follows:

$$d_0 = log\left(\frac{1}{R}\right)\frac{\tau V_s}{n_b \Delta h}, \tag{17}$$

where R is the reflection coefficient and V_s is the shear velocity.

4. Numerical Model and Experimental Setup

4.1. Numerical Model. The integrity coefficient $\beta = Z_2/Z_1$ in the pile length direction was used for damage definition, where $Z_i = \rho_i C_i A_i$ is the cross-sectional impedance, ρ_i is the density, C_i is the elastic wave velocity, and A_i is the cross-sectional area of the pile. Numerical models of two damaged piles with a cap and a damaged pile in soil were established to assess the 3D high-frequency interference effects caused by the cap. The impact locations on the top surface are shown in Figure 3.

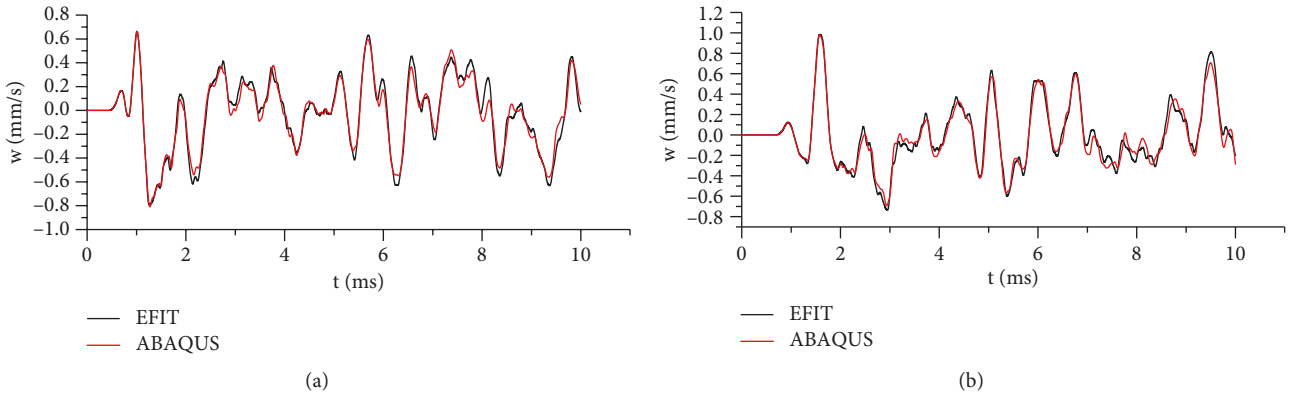

Figure 8: Comparison of velocities. (a) The W velocity at $y = 0.2$ m and $z = 3.0$ m. (b) The W velocity at $y = 0.2$ m and $z = 4.0$ m.

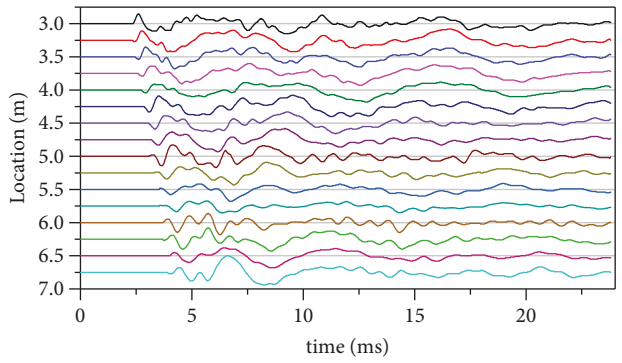

Figure 9: Velocity test data of the sensor array.

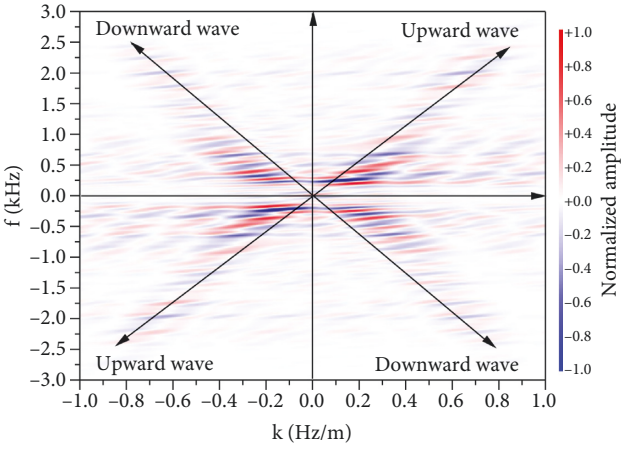

Figure 10: Results of the frequency-wavenumber domain analysis of the test data.

The two-pile model consists of two square piles and a cap. The computational models are shown in Figure 4. The EFIT numerical model of the two-pile model was constructed with the following parameters: $\Delta x = \Delta y = 0.01$ m, $\Delta z = 0.02$ m, and $\Delta t = 1\,\mu$s, and the impact parameters of equation (10) are as follows: $I = 1.0$, $t_0 = 0.5$ ms, and $r = 0.05$ m. The other parameters are listed in Tables 1 and 2.

The pile-soil model has the following soil parameters: S wave velocity = 100 m/s, Poisson's ratio $\nu = 0.35$, and density = 1600 kg/m^3. The soil location was at $x = -1$ m, 1 m, $y = -1$ m, 1 m, and $z = 4$–10 m. The computational domain is exhibited in Figure 4(b). The EFIT numerical model of the pile-soil model was constructed with the following parameters: the step size was $\Delta x = \Delta y = 0.02$ m, $\Delta z = 0.04$ m, and $t = 2\,\mu$s. The thickness of the PML was 0.4 m in the x- and y-directions and 0.8 m in the z-direction to meet the grid requirements of the PMLs. The other parameters are listed in Table 3 and Table 4.

4.2. Experimental Setup. A test model of the two-pile model was created for verification with the same parameters as the two-pile model. The lateral impact location was $Z_i = 1.0$ m (Figure 1), and the first sensor was located at $Z_s = 3.0$ m. The size of the middle hole is 13 × 13 cm, and the theoretical integrity coefficient β is 0.36. The number of sensors was 16, and the spacing of the sensors was 0.25 m. The sensor array configuration is shown in Figure 1, and the test setup is

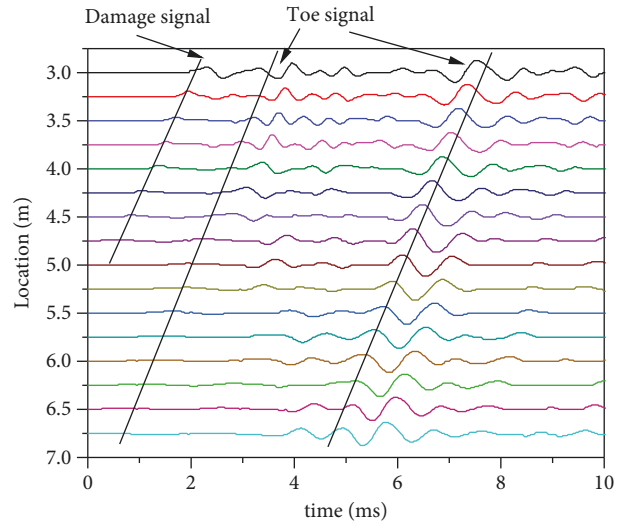

Figure 11: Upward velocities of the test data (A_i).

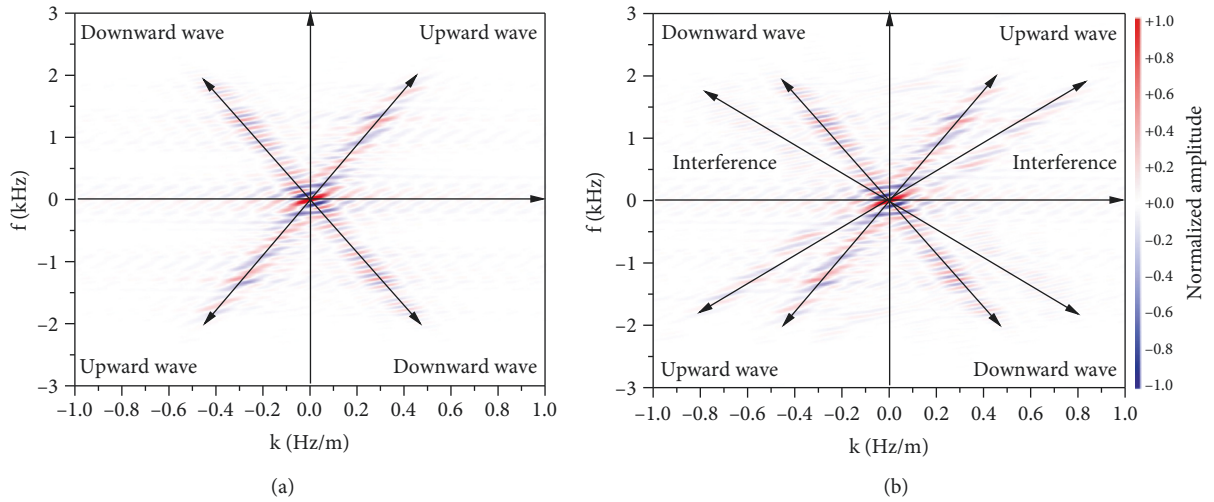

Figure 12: Results of frequency-wavenumber domain analysis (impact location $x = -0.1$ m). (a) Velocity data at A_i. (b) Velocity data at B_i.

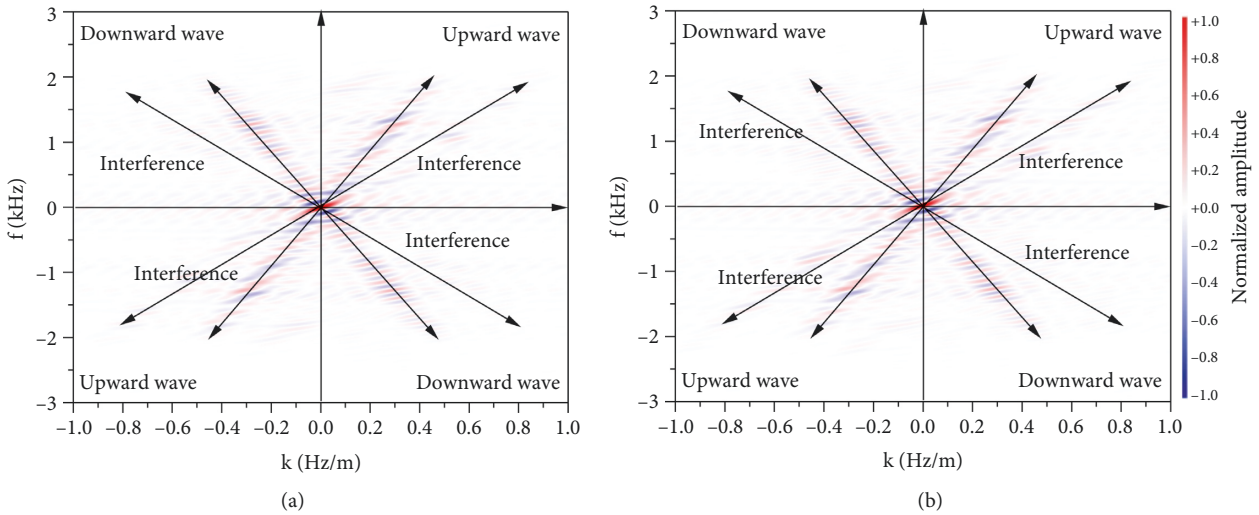

Figure 13: Results of frequency-wavenumber domain analysis ($y = 0.1$ m). (a) Velocity data at A_i. (b) Velocity data at B_i.

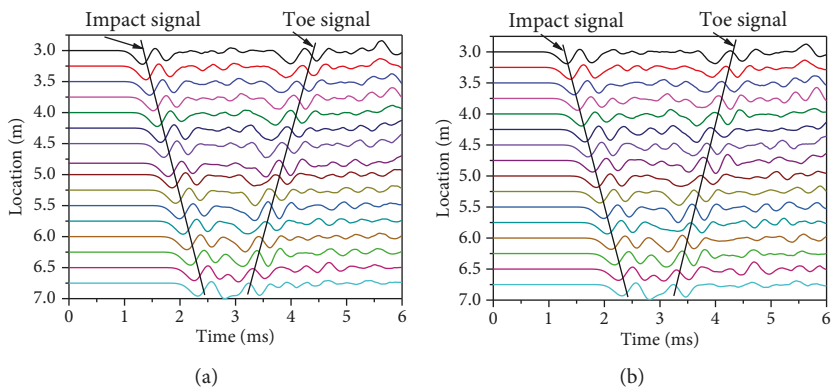

Figure 14: Raw velocity data. (a) Velocity data at A_i ($x = -0.1$ m). (b) Velocity data at A_i ($y = 0.1$ m).

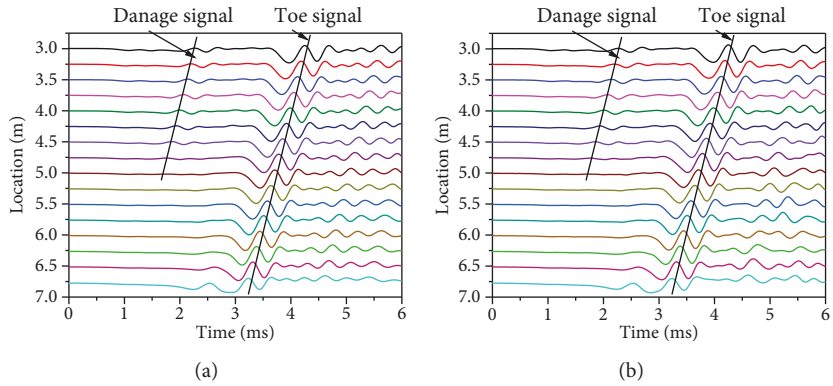

Figure 15: Upward velocity data. (a) Velocity data at A_i ($x = -0.1$ m). (b) Velocity data at A_i ($y = 0.1$ m).

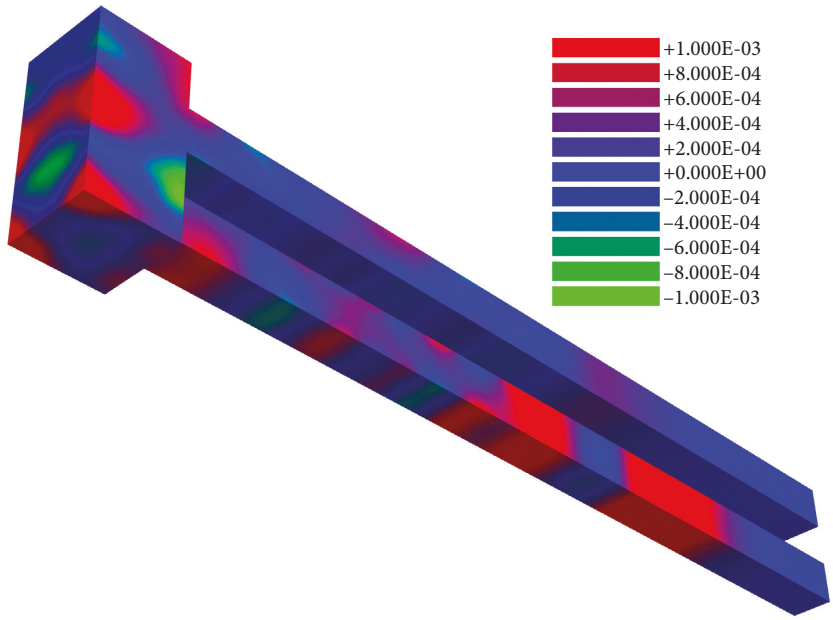

Figure 16: 3D contours of the impact on the top surface (time $t = 2.0$ ms).

shown in Figure 5. The acquisition instrument was a multichannel high-frequency tester with a maximum sampling frequency of 192 kHz.

5. Results and Discussion

5.1. Verification of EFIT. The EFIT results of the two-pile model were compared with the results of the Abaqus software to verify the accuracy and reliability of the numerical simulation [50]. Figures 6 and 7 show the Abaqus and EFIT models, respectively. The Abaqus and EFIT results are consistent. Figure 8 reveals that the peak values and phases of the wavelet are similar, indicating that the velocities of the Abaqus and EFIT models are consistent. These results verify the accuracy of the EFIT algorithm.

5.2. Verification of the FK Method. During the test, 16 sensors were used. The field detection layout is shown in Figure 5. When the pile is subjected to a lateral impact, bending and longitudinal waves are generated and propagated downward. The damage signals of these waves are difficult to detect using the traditional LST method, as shown in Figure 9. Figure 10 shows the results of the frequency-wavenumber domain analysis of the test data. Figure 11 shows the upward wavefield after wavefield separation. When the sensor is located close to the damage position ($Z_d = 4.5$ m), the amplitude of the damage signal is smaller due to the 3D effect. The proposed method can distinguish between the damage signal and the pile toe signal, as shown in Figure 11. The average arrival time of the damage signals indicates that the average location $Z_t = 4.46$ m is consistent with the actual location $Z_d = 4.5$ m.

5.3. Results of the Impact on the Top Surface. When the impact location is on the axis of symmetry ($x = -0.1$ m), one vibration mode occurs at sensors A_i, and two vibration modes occur at sensors B_i, as shown in Figure 12. In contrast, when the impaction location is not in the

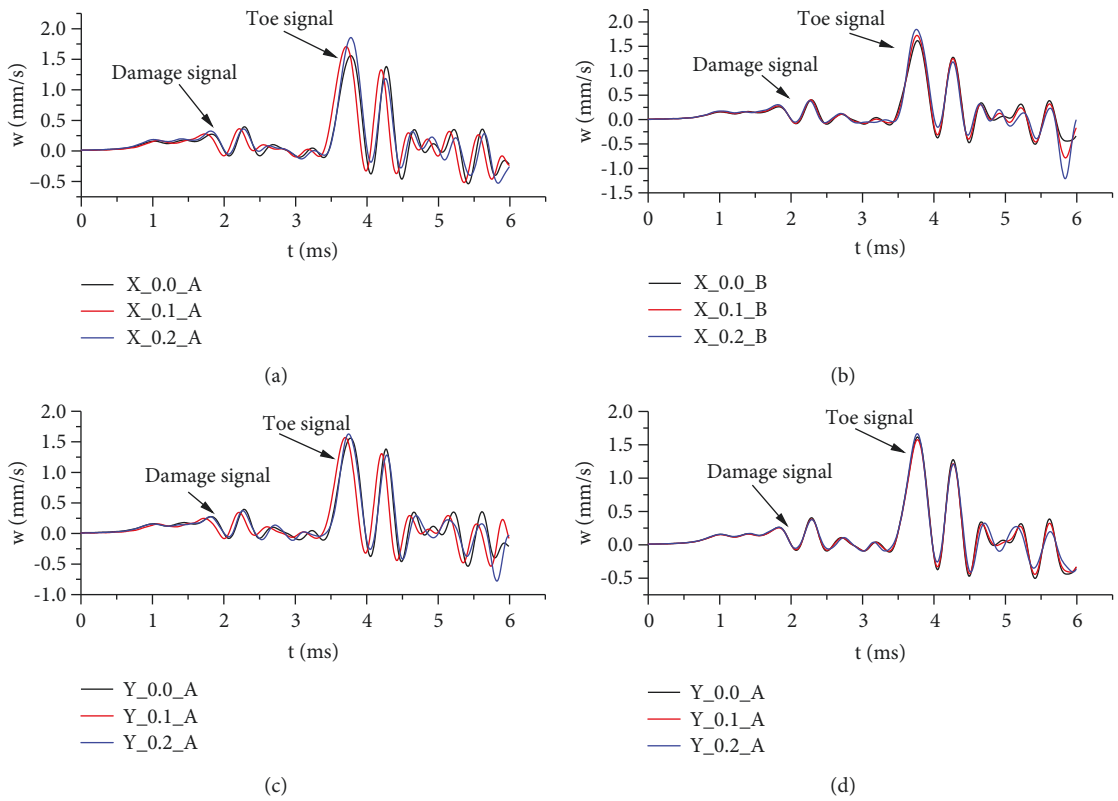

Figure 17: Upward velocities of different impact locations (sensor location $Z_s = 4.0$ m). (a) Upward velocities of A_i (impact location $x = 0.0$, -0.1, -0.2 m). (b) Upward velocities of B_i (impact location $x = 0.0$, -0.1, -0.2 m). (c) Upward velocities of A_i (impact location $y = 0.0$, 0.1, 0.2 m). (d) Upward velocities of B_i (impact location $y = 0.0$, 0.1, 0.2 m).

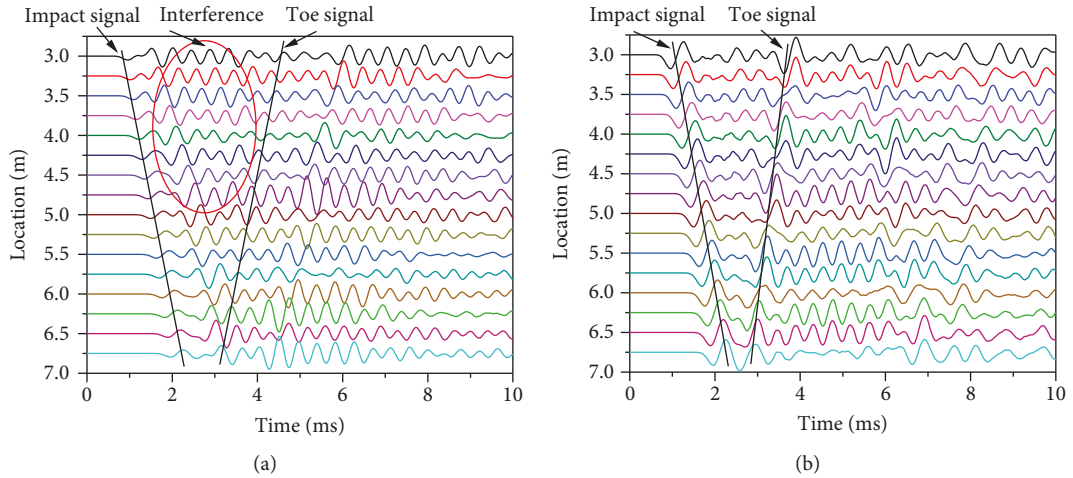

Figure 18: Raw velocity data. (a) Velocity data at A_i. (b) Velocity data at B_i.

symmetrical location ($y = 0.1$ m), there are two vibration modes at sensors A_i and B_i, as shown in Figure 13. The reason is that the sensors are not in the center of the bending plane. The hammering signal continues to reflect and propagate downward inside of the pile cap, and the asymmetric bending wave at the pile cap causes a slow-wave propagation speed. It is difficult to identify the reflected wave signals of the damage using the raw velocity data by the traditional LST method, as shown in Figure 14. Figure 15 and Figure 16 show that the reflected wave signals of the damage and pile toe are detected, indicating that using a sensor array can reduce the influences of the sensor location and impact location on the test results when the impact locations are on the top surface of the pile cap.

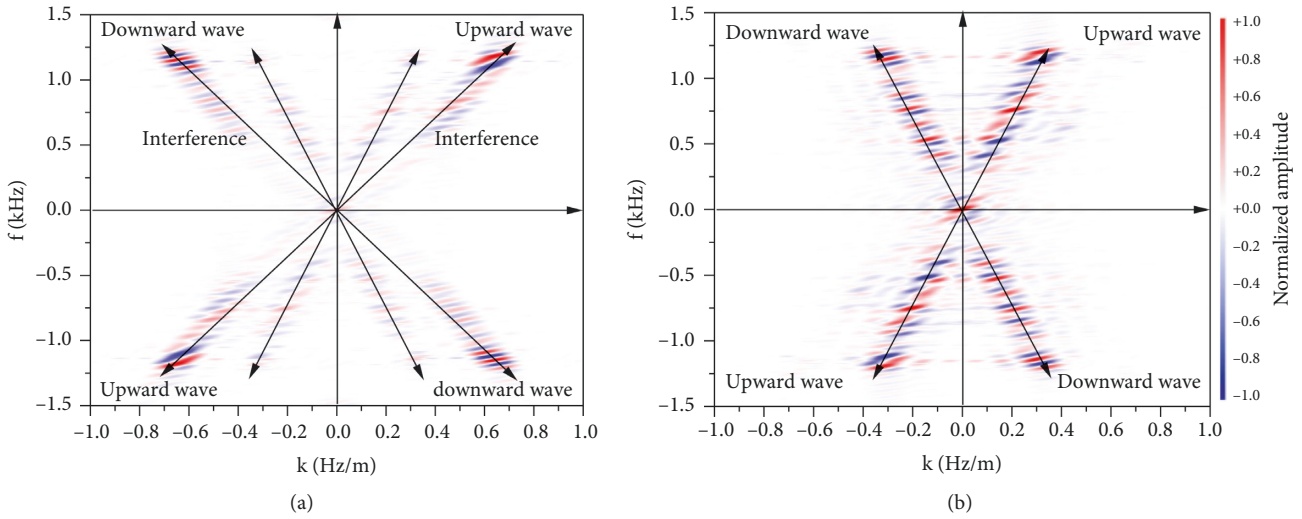

Figure 19: Results of the frequency-wavenumber domain analysis of the numerical data ($x = -0.1$ m). (a) Velocity data at A_i. (b) Velocity data at B_i.

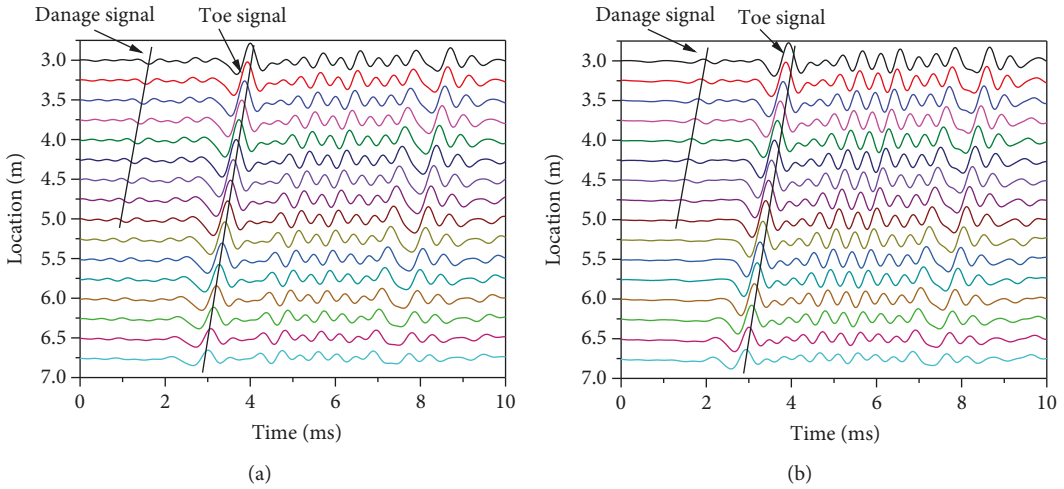

Figure 20: Upward velocity data. (a) Velocity data at A_i. (b) Velocity data at B_i.

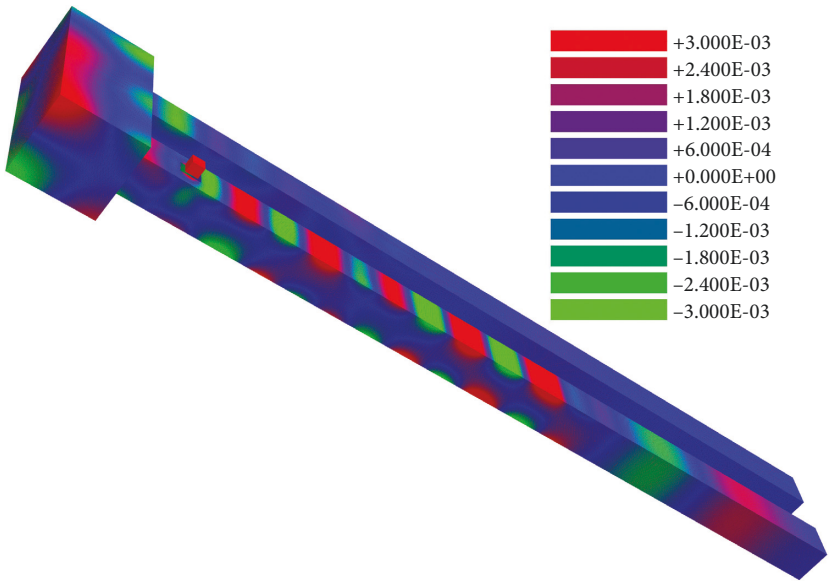

Figure 21: 3D contours of the impact on the concrete block (time $t = 2.0$ ms).

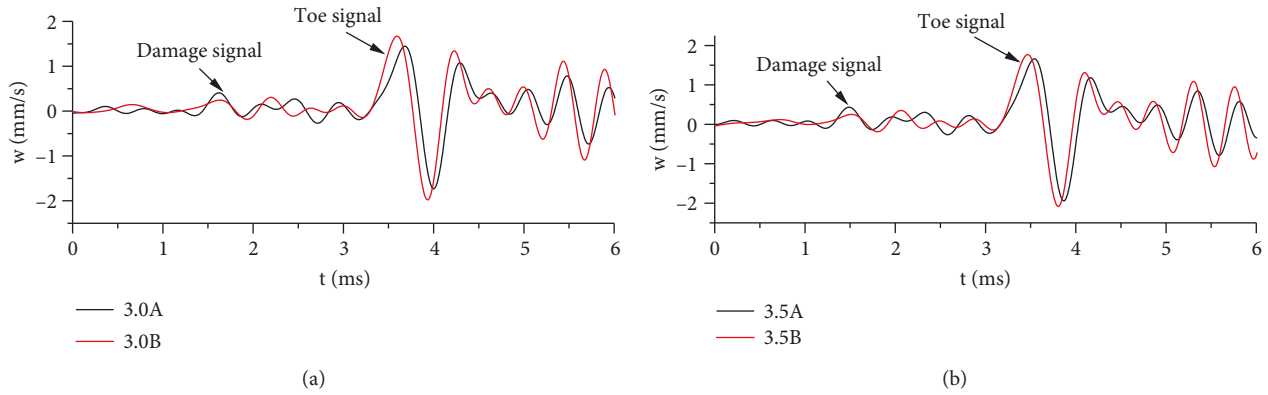

Figure 22: Upward velocities of different sensor locations. (a) Upward velocities of A_i and B_i (sensor location $Z_s = 3.0$ m). (b) Upward velocities of A_i and B_i (sensor location $Z_s = 3.5$ m).

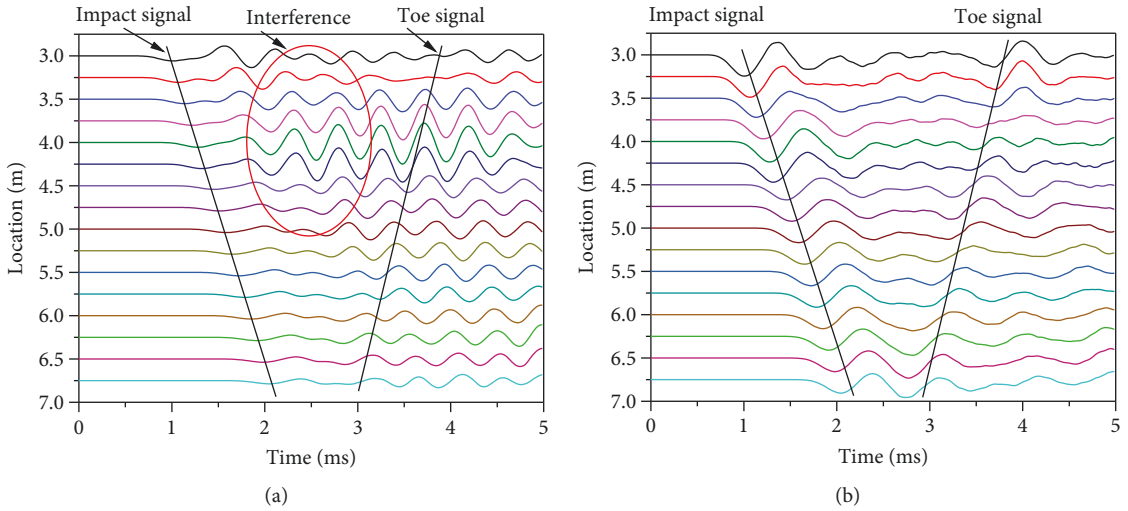

Figure 23: Raw velocity data. (a) Velocity data at A_i. (b) Velocity data at B_i.

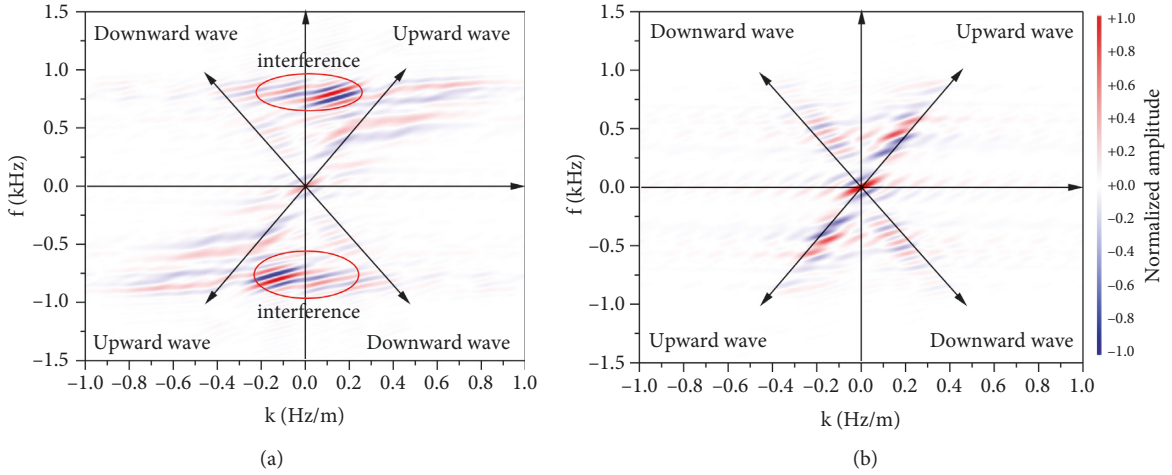

Figure 24: Results of the frequency-wavenumber domain analysis of the numerical data ($x = 0.1$ m). (a) Velocity data at A_i. (b) Velocity data at B_i.

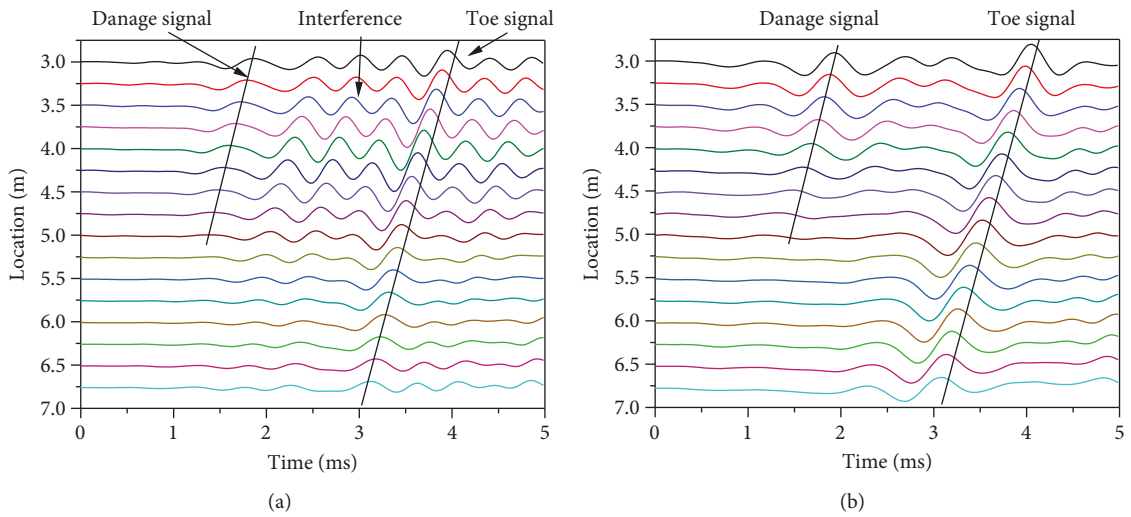

Figure 25: Upward velocity data. (a) Velocity data at A_i. (b) Velocity data at B_i.

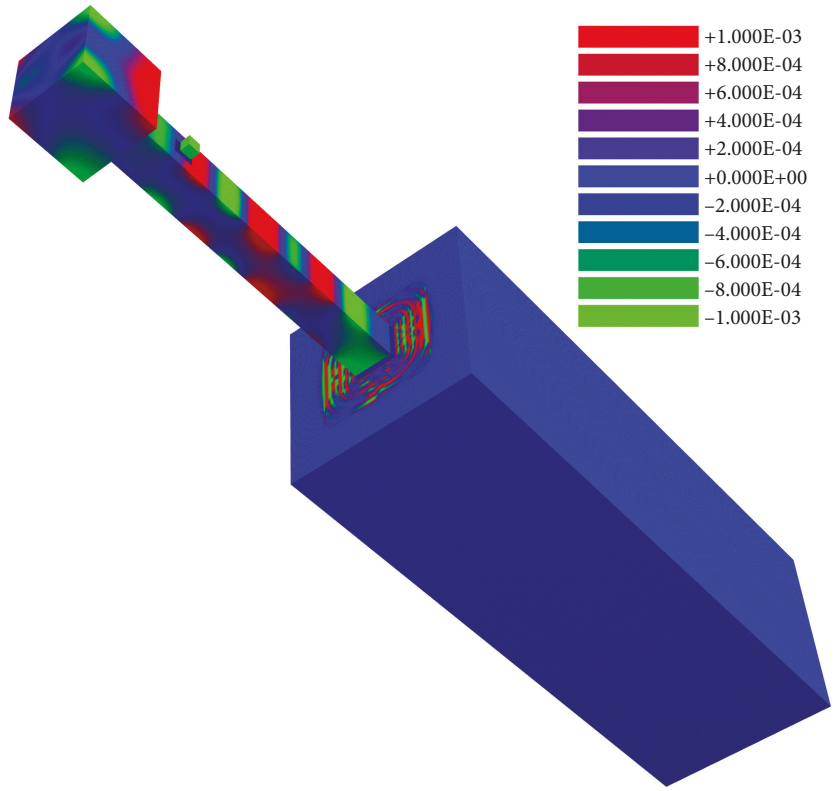

Figure 26: 3D contours of the impact on the concrete block (time $t = 2.0$ ms).

In the traditional LST method, the optimal distance between the striking point and the receiver is 0.5R–0.7 R when the impact location is on the top surface of the pile [12–14]. When two receivers are used, the impact location should be on the top surface of the pile cap, and the sensors should be placed on the bending plane relative to the impact location [46, 51]. Figure 17 exhibits different results of the upward velocities of different impact locations. The damage and toe signals can be distinguished, and there are no influences of the impact location and sensor location. There are slight differences in the damage and the toe signals when sensors A_i are not on the symmetry axis of the two-pile model, and the upward velocities of sensors B_i are almost the same. This result demonstrates that the use of a sensor array can reduce the influences of the sensor location and impact location.

5.4. Results of the Impact on the Concrete Block. When the impact occurs on the concrete block, only one vibration mode occurs at sensor B_i when the sensors are located on the

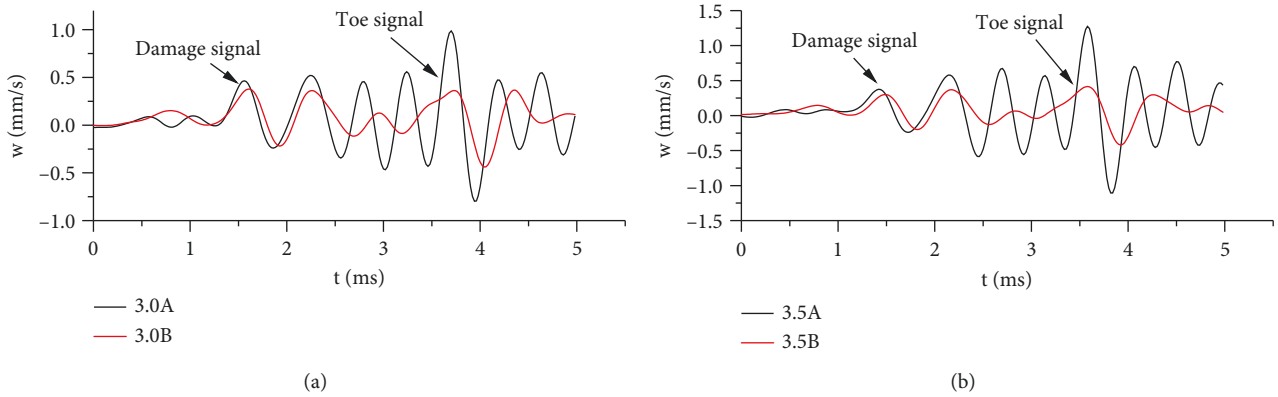

Figure 27: Upward velocities of different sensor locations. (a) Upward velocities of A_i and B_i (sensor location $Z_s = 3.0$ m). (b) Upward velocities of A_i and B_i (sensor location $Z_s = 3.5$ m).

bending plane relative to the impact location, and two vibration modes occur at sensor A_i. It is difficult to identify the reflected wave signals from the raw velocity data by the traditional LST method, as shown in Figure 18. Figures 19(a) and 18(a) show that the high-frequency interference is caused by the concrete block and is detected at location A_i. Figures 20 and 21 show that the high-frequency interference can be eliminated by the FK filtering method. When the impact is on the concrete block, the asymmetry of the pile cap has a negligible influence on the results. The upward velocity results of the different sensor locations (Figure 22) show that although the upward waves of A_i are affected by the high-frequency wave, the damage and toe signals can still be identified, in contrast to the results of B_i. It can be concluded that the sensors do not have to be placed on the bending plane relative to the impact location in the sensor array method. These findings indicate that using a sensor array can reduce the influence of the sensor location on the test results when the impact location is at the concrete block on the lateral surface of the pile.

5.5. Pile-Soil Model Results of the Impact on the Concrete Block. The results of the pile-soil model show the following. When the sensor is located on the bending plane relative to the impact location, only one vibration mode occurs at sensors B_i. The FK domain results show that the interference signal is more pronounced, and the frequency bandwidth of the upward wave is wider at sensors A_i than at sensors B_i. It is difficult to identify the meaningful reflected wave signals from the raw velocity data by the traditional LST method, as shown in Figure 23. Figures 24–26 show that the high-frequency interference can be eliminated by the FK filtering method. The interference of the time-domain signal is caused by the wider bandwidth of the upward wave. Since the reflected wave of the interference signal is received later at sensors A_i, the interference signal does not affect the identification of the defect signal. Due to the scattering effect of the soil and the influence of high-frequency waves (Figure 27), the upward wave of A_i shows high-frequency oscillations caused by the concrete block, and the toe signal is affected by the high-frequency wave, in contrast to the results of B_i. Since the upward waves of B_i occur on the bending plane relative to the impact location, the influence of high-frequency oscillations is small. These results indicate that the use of a sensor array reduces the influence of the sensor location on the results.

6. Conclusions

An analysis method based on FK analysis, a filtering window function, and a sensor array was proposed for integrity assessments of platform-pile systems. Different impact locations and sensor configurations were considered. The following conclusions were obtained:

(1) A comparison of the results of numerical simulations and experiments indicated the accuracy and reliability of the proposed analysis method for integrity testing.

(2) Two wave vibration modes were observed because of the interference signal. Since the sensors were not located at the center of the bending plane, the asymmetric bending waves at the pile cap resulted in slow-wave propagation speed. Placing the sensors at the bending plane relative to the impact location is the optimum choice to reduce the influence of the interference signal.

(3) The FK filtering method eliminated the propagation of the high-frequency interference. When the impact was on the concrete block, the asymmetry of the pile cap had a negligible influence on the results.

(4) Using a sensor array can reduce the influence of the sensor location on the test results and minimize the requirements for determining the location of the impact point and sensors in traditional LST methods, improving their applicability.

Data Availability

The data used to support the findings of this study are included within the article.

Conflicts of Interest

The authors declare that they have no conflicts of interest.

Acknowledgments

The authors are grateful for the financial support from the National Natural Science Foundation of China (grant number: 11672338) and the Science and Technology Program of Guangzhou, China (grant number: 201904010332).

References

[1] A. G. Davis, "Nondestructive evaluation of existing deep foundations," *Journal of Performance of Constructed Facilities*, vol. 9, no. 1, pp. 57–74, 1995.

[2] L. D. Olson, M. Liu, and M. F. Aouad, "Borehole NDT techniques for unknown subsurface bridge foundation testing," in *Nondestructive Evaluation of Bridges and Highways*, International Society for Optics and Photonics, Washington, DC, USA, 1996.

[3] B. H. Hertlein and W. H. Walton, "Assessment and reuse of old foundations," *Transportation Research Record: Journal of the Transportation Research Board*, vol. 1736, no. 1, pp. 48–52, 2000.

[4] G. Campione, F. Cannella, and L. Cavaleri, "Shear and flexural strength prediction of corroded R.C. beams," *Construction and Building Materials*, vol. 149, pp. 395–405, 2017.

[5] W. Shao, D. Shi, J. Jiang, and Y. Chen, "Time-dependent lateral bearing behaviour of corrosion-damaged RC pipe piles in marine environments," *Construction and Building Materials*, vol. 157, pp. 676–684, 2017.

[6] L. Chen and A. Mathai, "Numerical analysis of the deformation performance of monopile under wave and current load," *Energies*, vol. 13, no. 23, p. 6431, 2020.

[7] L. Wang, C. Liu, and L. Wang, "A simplified method for assessing the dynamic behaviour of a pile in layered saturated soils that considers current scour," *Computers and Geotechnics*, vol. 128, Article ID 103831, 2020.

[8] E. B. Flynn, M. D. Todd, A. J. Croxford, B. W. Drinkwater, and P. D. Wilcox, "Enhanced detection through low-order stochastic modeling for guided-wave structural health monitoring," *Structural Health Monitoring*, vol. 11, no. 2, pp. 149–160, 2012.

[9] T. Clarke, F. Simonetti, and P. Cawley, "Guided wave health monitoring of complex structures by sparse array systems: influence of temperature changes on performance," *Journal of Sound and Vibration*, vol. 329, no. 12, pp. 2306–2322, 2010.

[10] S.-H. Ni, Y.-H. Huang, K.-F. Lo, and J.-Jy Charng, "Estimating the flaw size in drilled shafts using an impulse response method," *KSCE Journal of Civil Engineering*, vol. 15, no. 7, pp. 1197–1207, 2011.

[11] S. Sajid and L. Chouinard, "Impulse response test for condition assessment of concrete: a review," *Construction and Building Materials*, vol. 211, pp. 317–328, 2019.

[12] C. Zheng, G. P. Kouretzis, X. Ding, H. Liu, and H. G. Poulos, "Three-dimensional effects in low-strain integrity testing of piles: analytical solution," *Canadian Geotechnical Journal*, vol. 53, no. 2, pp. 225–235, 2015.

[13] C. Zheng, L. Hong, D. Xuanming, and K. George, "Three-dimensional effects in low-strain integrity testing of large diameter pipe piles," *Journal of Engineering Mechanics*, vol. 142, no. 9, Article ID 04016064, 2016.

[14] Y. Chow, K. K. Phoon, W. F. Chow, and K. Y. Wong, "Low strain integrity testing of piles: three-dimensional effects," *Journal of Geotechnical and Geoenvironmental Engineering*, vol. 129, no. 11, pp. 1057–1062, 2003.

[15] Y.-H. Huang and S.-H. Ni, "Experimental study for the evaluation of stress wave approaches on a group pile foundation," *NDT & E International*, vol. 47, pp. 134–143, 2012.

[16] H.-Y. Chai, K.-K. Phoon, and D.-J. Zhang, "Effects of the source on wave propagation in pile integrity testing," *Journal of Geotechnical and Geoenvironmental Engineering*, vol. 136, no. 9, pp. 1200–1208, 2010.

[17] X. Ding, H. Liu, and B. Zhang, "High-frequency interference in low strain integrity testing of large-diameter pipe piles," *Science China Technological Sciences*, vol. 54, no. 2, pp. 420–430, 2011.

[18] S. Kenai and R. Bahar, "Evaluation and repair of Algiers new airport building," *Cement and Concrete Composites*, vol. 25, no. 6, pp. 633–641, 2003.

[19] J.-Y. Zhang and X. Lei, "Numerical modeling of parallel seismic method for detecting existing piles in layered soil," *Soils and Foundations*, vol. 58, no. 1, pp. 134–145, 2018.

[20] S.-T. Liao, J.-H. Tong, C.-H. Chen, and T.-T. Wu, "Numerical simulation and experimental study of parallel seismic test for piles," *International Journal of Solids and Structures*, vol. 43, no. 7-8, pp. 2279–2298, 2006.

[21] S.-H. Ni, Y.-H. Huang, X.-M. Zhou, and K.-F. Lo, "Inclination correction of the parallel seismic test for pile length detection," *Computers and Geotechnics*, vol. 38, no. 2, pp. 127–132, 2011.

[22] E. Niederleithinger, "Improvement and extension of the parallel seismic method for foundation depthmeasurement," *Soils and Foundations*, vol. 52, no. 6, pp. 1093–1101, 2012.

[23] Z. T. Lu, Z. L. Wang, and D. J. Liu, "A study on the application of the parallel seismic method in pile testing," *Soil Dynamics and Earthquake Engineering*, vol. 55, pp. 255–262, 2013.

[24] E. Uncuoğlu and M. Laman, "Numerical modelling of short pile behaviour subjected to lateral load," *European Journal of Environmental and Civil Engineering*, vol. 16, no. 2, pp. 204–235, 2012.

[25] H. Wang, T.-P. Chang, and J.-J. Wang, "Response analysis of concrete piles subjected to lateral impact," *Journal of Marine Science and Technology*, vol. 18, no. 6, p. 9, 2010.

[26] J. Yang, X.-L. Sun, De-C. Bian, and J.-X. Shao, "Large-scale model test for detecting pile defects using the parallel seismic method," *Soil Dynamics and Earthquake Engineering*, vol. 139, Article ID 106300, 2020.

[27] L.-Z. Hu and G. A. McMechan, "Wave-field transformations of vertical seismic profiles," *Geophysics*, vol. 52, no. 3, pp. 307–321, 1987.

[28] M. D. Rogge and C. A. Leckey, "Characterization of impact damage in composite laminates using guided wavefield imaging and local wavenumber domain analysis," *Ultrasonics*, vol. 53, no. 7, pp. 1217–1226, 2013.

[29] M. Ruzzene, "Frequency–wavenumber domain filtering for improved damage visualization," *Smart Materials and Structures*, vol. 16, no. 6, p. 2116, 2007.

[30] R. Zhu, G. Huang, and F. Yuan, "Fast damage imaging using the time-reversal technique in the frequency–wavenumber domain," *Smart Materials and Structures*, vol. 22, no. 7, Article ID 075028, 2013.

[31] E. B. Flynn, S. Y. Chong, G. J. Jarmer, and J.-R. Lee, "Structural imaging through local wavenumber estimation of guided waves," *NDT & E International*, vol. 59, pp. 1–10, 2013.

[32] F. Schubert, P. Alexander, and K. Bernd, "The elastodynamic finite integration technique for waves in cylindrical geometries," *Journal of the Acoustical Society of America*, vol. 104, no. 5, pp. 2604–2614, 1998.

[33] F. Schubert and B. Köhler, "Three-dimensional time domain modeling of ultrasonic wave propagation in concrete in explicit consideration of aggregates and porosity," *Journal of Computational Acoustics*, vol. 9, no. 4, pp. 1543–1560, 2001.

[34] F. Schubert, "Numerical time-domain modeling of linear and nonlinear ultrasonic wave propagation using finite integration techniques––theory and applications," *Ultrasonics*, vol. 42, no. 1-9, pp. 221–229, 2004.

[35] J. Bingham and M. Hinders, "3D elastodynamic finite integration technique simulation of guided waves in extended built-up structures containing flaws," *Journal of Computational Acoustics*, vol. 18, no. 2, pp. 165–192, 2010.

[36] S. Chaillat, M. Bonnet, and J.-F. c. Semblat, "A multi-level fast multipole BEM for 3-D elastodynamics in the frequency domain," *Computer Methods in Applied Mechanics and Engineering*, vol. 197, no. 49-50, pp. 4233–4249, 2008.

[37] Z. Ge and X. Chen, "Wave propagation in irregularly layered elastic models: a boundary element approach with a global reflection/transmission matrix propagator," *Bulletin of the Seismological Society of America*, vol. 97, no. 3, pp. 1025–1031, 2007.

[38] W. M. Ostachowicz, "Damage detection of structures using spectral finite element method," *Computers & Structures*, vol. 86, no. 3-5, pp. 454–462, 2008.

[39] Z. Tian, L. Yu, C. Leckey, and J. Seebo, "Guided wave imaging for detection and evaluation of impact-induced delamination in composites," *Smart Materials and Structures*, vol. 24, no. 10, Article ID 105019, 2015.

[40] E. J. Candes and D. L. Donoho, *Curvelets: A Surprisingly Effective Nonadaptive Representation for Objects with Edges*, Stanford Univ Ca Dept of Statistics, Stanford, California, 2000.

[41] E. Candes, L. Demanet, D. Donoho, and L. Ying, "Fast discrete curvelet transforms," *Multiscale Modeling & Simulation*, vol. 5, no. 3, pp. 861–899, 2006.

[42] N. E. Huang, Z. Shen, S. R. Long et al., "The empirical mode decomposition and the Hilbert spectrum for nonlinear and non-stationary time series analysis," *Proceedings of the Royal Society of London. Series A: Mathematical, Physical and Engineering Sciences*, vol. 454, pp. 903–995, 1971.

[43] C. A. Leckey, M. D. Rogge, C. A. Miller, and M. K. Hinders, "Multiple-mode Lamb wave scattering simulations using 3D elastodynamic finite integration technique," *Ultrasonics*, vol. 52, no. 2, pp. 193–207, 2012.

[44] P. Fellinger, R. Marklein, K. J. Langenberg, and S. Klaholz, "Numerical modeling of elastic wave propagation and scattering with EFIT—elastodynamic finite integration technique," *Wave Motion*, vol. 21, no. 1, pp. 47–66, 1995.

[45] M. Kindelan, A. Kamel, and P. Sguazzero, "On the construction and efficiency of staggered numerical differentiators for the wave equation," *Geophysics*, vol. 55, no. 1, pp. 107–110, 1990.

[46] M. Fu and M. Lin, "A study on integrity testing for platform-pile systems considering wave propagation," *Mathematical Problems in Engineering*, vol. 2022, Article ID 1431774, 21 pages, 2022.

[47] P. Moczo, K. Jozef, V. Václav, R. J. Archuleta, and L. Halada, "3D heterogeneous staggered-grid finite-difference modeling of seismic motion with volume harmonic and arithmetic averaging of elastic moduli and densities," *Bulletin of the Seismological Society of America*, vol. 92, no. 8, pp. 3042–3066, 2002.

[48] J. Kristek, P. Moczo, and R. J. Archuleta, "Efficient methods to simulate planar free surface in the 3D 4th-order staggered-grid finite-difference schemes," *Studia Geophysica et Geodaetica*, vol. 46, no. 2, pp. 355–381, 2002.

[49] C. Marcinkovich and K. Olsen, "On the implementation of perfectly matched layers in a three-dimensional fourth-order velocity-stress finite difference scheme," *Journal of Geophysical Research: Solid Earth*, vol. 108, no. B5, 2003.

[50] G. Abaqus, *Abaqus 6.11*, Dassault Systemes Simulia Corporation, Providence, RI, USA, 2011.

[51] H. Liu, W. Wu, G. Jiang, M. H. E. Naggar, M. Guoxiong, and L. Rongzhu, "Benefits from using two receivers for interpretation of low-strain integrity tests on pipe piles," *Canadian Geotechnical Journal*, vol. 56, no. 10, pp. 1433–1447, 2019.